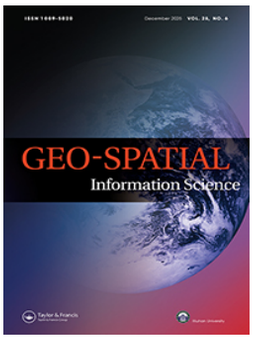

Geo-spatial Information Science

ISSN: 1009-5020 (Print) 1993-5153 (Online) Journal homepage: www.tandfonline.com/journals/tgsi20

Modified ionosphere delay fitting model with atmosphere uncertainty grids for wide-area real-time positioning

Bobin Cui, Jungang Wang, Pan Li, Jiahuan Hu, Xiang Zuo & Longjiang Tang

To cite this article: Bobin Cui, Jungang Wang, Pan Li, Jiahuan Hu, Xiang Zuo & Longjiang Tang (2025) Modified ionosphere delay fitting model with atmosphere uncertainty grids for wide-area real-time positioning, Geo-spatial Information Science, 28:6, 3211-3229, DOI: 10.1080/10095020.2024.2440091

To link to this article: https://doi.org/10.1080/10095020.2024.2440091

Published online: 17 Jan 2025.

GEO-SPATIAL INFORMATION SCIENCE
2025, VOL. 28, NO. 6, 3211–3229
https://doi.org/10.1080/10095020.2024.2440091

Taylor & Francis
Taylor & Francis Group

Modified ionosphere delay fitting model with atmosphere uncertainty grids for wide-area real-time positioning

Bobin Cui [a,b], Jungang Wang [c], Pan Li [a], Jiahuan Hu [d], Xiang Zuo [c] and Longjiang Tang [c,e]

[a]College of Geology Engineering and Geomatics, Chang'an University, Xi'an, China; [b]Smart-BDS Shaanxi University Engineering Research Center, Chang'an University, Xi'an, China; [c]Institut für Geodäsie und Geoinformationstechnik, Technische Universität Berlin, Berlin, Germany; [d]Department of Earth and Space Science and Engineering, York University, Toronto, Canada; [e]Space Geodetic Techniques, Deutsches GeoForschungsZentrum GFZ, Telegrafenberg, Potsdam, Germany

ABSTRACT

Precise atmospheric delay and proper constraints are critical for achieving rapid convergence and accurate positioning. However, ionospheric delay models over wide-area face challenges due to significant spatial and temporal variations, impacting real-time correction precision. To address this, we propose a novel ionospheric slant delay fitting model that adaptively selects the optimal reference path within coverage areas, describing differences between the reference propagation path and others through trigonometric functions. With ten coefficients, the model surpasses legacy polynomial fitting accuracy. Using a 166-station, 150 km-spaced European networks for atmospheric delays and 113 external stations for validation, our model achieves a 59.6% standard deviation reduction compared to the legacy model. Compared to the legacy ionospheric delay model, new model positioning convergence time (≤10 cm) accelerates by 37.7% and 34.2% for horizontal and vertical components, respectively. Meanwhile, two 2° × 2° uncertainty grids, generated from tropospheric and ionospheric delay fitting residuals at 15-min intervals, accurately describe fitting performance in all coverage areas with a maximum of 475 points. Adaptive constraints from uncertainty grids can reduce convergence time by 42.1% and 28.8% for horizontal and vertical, surpassing three-time modeling sigma solutions. These findings underscore the effectiveness of our novel ionospheric delay fitting model and the associated uncertainty grids in providing precise information across extensive regions with minimal coefficients.

ARTICLE HISTORY
Received 31 March 2024
Accepted 4 December 2024

KEYWORDS
Precise point positioning (PPP); slant ionospheric delay; atmosphere uncertainty information; large-area augmentation

1. Introduction

As a major error source in global navigation satellite systems (GNSSs), atmospheric delays must be carefully handled in high-precision GNSS applications, either by calibrating using external products or by estimating as unknown parameters. The latter, however, causes a large convergence time up to 30 min in the precise point positioning (PPP) solutions (Ge et al. 2021; Ji et al. 2022). Therefore, introducing external precise atmospheric delay information with the proper weight is critical to achieve rapid convergence for the real-time PPP solutions with ambiguity resolution (AR) (Teunissen and Khodabandeh 2014).

Atmospheric delay includes tropospheric and ionospheric delays, and the tropospheric delay can be modeled in large areas with a precision of 2 cm (Cui et al. 2022; Li et al. 2022b; Xu et al. 2023) or corrected with precise numerical weather model (Hobiger et al. 2008; Lu et al. 2017). In contrast, the ionospheric delay is difficult to be estimated or described accurately by the function models. Usually, the first-order ionospheric delay can be eliminated with the ionosphere-free combination or estimated as a parameter in positioning with the un-differenced and un-combined (UDUC) PPP model. The latter is more suitable for multi-frequency PPP real-time kinematic (PPP-RTK) applications (Hirokawa, Fernández-Hernández, and Reynolds 2021; Wübbena, Schmitz, and Bagge 2005).

At present, the International GNSS Service (IGS) releases real-time/rapid/final global ionosphere maps (GIM) based on a vertical spherical harmonic model with different time latencies to provide ionospheric delay corrections. The precision of real-time ionospheric delay GIM varies from 2 to 7 total electron content units (TECU), with a 15-min update and a latency of less than 5 min (Hernández-Pajares et al. 2017; Liu et al. 2021; Psychas et al. 2019). However, meeting the demands of rapid positioning over large areas remains a challenge. Furthermore, a Quasi-4-dimensional ionospheric model has been proposed, which defines appropriate grids in latitude, longitude, elevation, and azimuth to generate a four-dimensional matrix, achieving a precision of 0.5 TECU in Europe (Gu et al. 2022). Additionally, an alternative approach involves directly interpolating precise ionospheric

CONTACT Pan Li lipan@chd.edu.cn

delays from nearby reference stations to users (Li et al. 2022b). Nevertheless, as highlighted by Cui et al. (2023), the transmission of massive corrections in grid or interpolation forms relies on stable and high network capabilities. This poses a challenge in wide-area services, and a careful trade-off between the number of parameters and the represented precision must be considered, taking into account the limitations of satellite communication capabilities. In contrast, satellite communication is the preferred choice for wide-area services such as intercontinental communication due to its ability to handle wide-area with less transmission burden.

Currently, vertical TEC mathematical function models are commonly used in wide-area to describe ionospheric delay variations, including trigonometric series functions (Yuan et al. 2008) and spherical cap harmonic functions (Liu et al. 2010). However, the precision is affected by the mapping function or limited by the distribution and density of station networks. Although an improved mapping function considering the slant delay elevation and azimuth angles was proposed by Chen et al. (2022), the mapping function from slant to vertical delay could still introduce errors and impact the modeling precision. Therefore, in high-precision ionospheric delay modeling, satellite-wise slant instead of vertical ionospheric delays are preferred to be processed (Cabinst Office 2020; Li et al. 2021; Tao and Jan 2015). Hence, a fitting model that considers ionospheric slant delays in accordance with propagation properties on a satellite-wise basis is more suitable for large-scale applications. Achieving real-time high-frequency updates, such as every 30 s, is still challenging due to limitations in real-time communication and data volume (Nadarajah et al. 2018). Therefore, satellite-wise interpolation models or grids over wide-area are not widely used. Instead, the polynomial fitting model remains the most commonly adopted approach for real-time wide-area augmentation services (Hirokawa, Fernández-Hernández, and Reynolds 2021). A modified spherical harmonic and generalized trigonometric series function was proposed by Liu et al. (2010), which enlarges the model coverage areas and improves the precision of modeling. Additionally, modified single-layer fitting models (Li, Zhang, and Ge 2011) or dual-layer vertical models (Rovira-Garcia et al. 2021) have been successively proposed to enhance the modeling performance. High-precision ionospheric delay fitting models are usually performed in small (10–50 km) or middle coverage areas (30–300 km) with calm ionospheric delay activity (Boisits, Glaner, and Weber 2020; Cui et al. 2023; Manzoni et al. 2024; Teunissen, Odijk, and Zhang 2010; Zhang, Teunissen, and Odijk 2011). Unlike the interpolation model, the performance of the fitting model has a strong correlation not only with the density of the stations but also with the size of the coverage area. Therefore, it is challenging to present regional variation information in the entire European region using mathematical functions, which are typically smooth and continuous.

Despite the availability of various models and forms to characterize atmospheric delays, an unbiased description of the actual atmospheric delay is still unachievable in large-area services (Psychas, Khodabandeh, and Teunissen 2021). Therefore, a constraint is typically introduced to describe the precision of received external atmosphere corrections, namely atmosphere uncertainty (Lyu, Xiang, Soja, et al. 2023; Lyu, Xiang, Zhang, et al. 2023). Currently, there are three methods available to apply these corrections: atmosphere-free, weighted, and empirical solutions. However, the constant or empirical uncertainty information is difficult to meet wide-area requirements, and thus, too-tight or -loose constraints could result in longer convergence times and worse ambiguity resolution (Bilitza 2018; Teunissen, Odijk, and Zhang 2010; Wang et al. 2020; Zhang, Teunissen, and Odijk 2011; Zhang et al. 2022). To determine an appropriate constraint value for real-time wide-area services, namely the weighted solution, distance-related standard error functions and power functions with constant coefficients have been proposed, but they are only suitable in specific areas (Nadarajah et al. 2018, Zha et al. 2021). For wide-area, uncertainty grids (Banville et al. 2022) and inter-satellite cross-verification error function (Li et al. 2022b) methods have been proposed for the adaptive determination of ionosphere uncertainty information. However, they require a dense server network, and the user performance depends on station distribution and network communication capabilities. Currently, there is limited emphasis on developing real-time fitting models with applicable uncertainty information for large areas. Additionally, current research mainly focuses on providing the uncertainty for the ionospheric delay but rarely considers the uncertainty for the tropospheric delay.

Therefore, both precise ionospheric delay correction and the proper corresponding atmospheric delay uncertainty are essential for rapid positioning applications. In this study, we propose a new ionospheric slant delay fitting model to achieve better performance in wide-area by introducing a trigonometric model to describe the elevation and azimuth angle differences between the optimized reference propagation path and others, which confirms the strong correlation between the ionospheric delay propagation path length and magnitude. Moreover, based on the generated tropospheric and ionospheric fitting residuals, two sets of atmosphere uncertainty grids are further introduced separately to describe the accuracy of the tropospheric and ionospheric delay fitting models, providing more proper constraints for positioning. These models are

designed to be more applicable to wide-area augmentation satellite-based one-way communication, requiring a relatively smaller data volume.

The new ionosphere fitting model and atmosphere uncertainty information are investigated and analyzed in this paper. First, the methods for atmospheric delay modeling and uncertainty grid generation are presented. The detailed processing strategies of the experimental and observational data are presented then, followed by the analysis of atmospheric precision of the fitting models and the uncertainty grid. Finally, the PPP-AR results constrained under the proposed model are given, and the conclusions are drawn.

2. Methodology

In this section, the procedures applied in atmospheric delay deriving and modeling, and positioning verification are described. Carrier phase L and pseudo-range P observations between satellite s and receiver r on frequency f are expressed as,

$$L_{r,f}^{s} = \rho_r^s + c(dt_r - dt^s) + Z_r^s - \kappa_f I_{r,1}^s + \lambda_f N_f + \lambda_f \left(b_{r,f} + b_f^s\right) + \varepsilon_{L,f} \tag{1}$$

$$P_{r,f}^{s} = \rho_r^s + c(dt_r - dt^s) + Z_r^s + \kappa_f I_{r,1}^s + c\left(d_{r,f} + d_f^s\right) + \varepsilon_{P,f} \tag{2}$$

where ρ_r^s is the geometry range from satellite to receiver; dt^s and dt_r are the satellite and receiver clock offsets, respectively; Z_r^s is the tropospheric delay; $I_{r,1}^s$ is the ionospheric delay of the signal path at frequency 1 and $\kappa_f = f_1^2/f_f^2$; λ_f is the wavelength; N_f is the integer ambiguity; $b_{r,f}$ and b_f^s are the receiver- and satellite-dependent uncalibrated phase delays (UPD), respectively; $d_{r,f}$ and d_f^s are the code biases of the receiver and satellite, respectively; $\varepsilon_{P,f}$ and $\varepsilon_{L,f}$ are the measurement noise of the pseudo-range and carrier phase observations, respectively.

In multi-GNSS observations, it is necessary to consider the inter-system bias (ISB) between different systems. However, for GLONASS satellites, the inter-frequency bias (IFB) must be introduced instead of ISB parameter due to their utilization of frequency division multiple access (FDMA) technology. In this study, the ambiguity resolution is only conducted on GPS and Galileo satellites, while BDS and GLONASS are processed as float solutions. By utilizing real-time satellite precise orbits, clock products, and model corrections, Equations (1) and (2) can be simplified and reparameterized following Teunissen and Khodabandeh (2014), Zhang, Chen, and Yuan (2018), and Zhang et al. (2022):

$$\begin{aligned} l_{r,j}^{s,Sys} &= -u_r^s \cdot \Delta r - c \cdot d\bar{t}_r + \lambda_j^{Sys} B_{r,j}^{s,Sys} - \kappa_j^{Sys} \cdot \hat{I}_{r,1}^{s,Sys} \\ &\quad + m_r^{s,Sys} \cdot ZWD_r + ISB^{Sys} + IFB^s + \varepsilon_{l,j}^{s,Sys} \\ p_{r,j}^{s,Sys} &= -u_r^s \cdot \Delta r - c \cdot d\bar{t}_r + c \cdot \kappa_j^{Sys} \cdot d_{r,j} + \kappa_j^{Sys} \cdot \hat{I}_{r,1}^{s,Sys} \\ &\quad + m_r^{s,Sys} \cdot ZWD_r + ISB^{Sys} + IFB^s + \varepsilon_{p,j}^{s,Sys} \end{aligned} \tag{3}$$

where $l_{r,j}^s$ and $p_{r,j}^s$ denote the observed-minus-computed (OMC) carrier phase and pseudo-range observations, respectively; $d\bar{t}_r$ is the receiver clock after merging the receiver pseudorange delay; $\hat{I}_{r,1}^{s,Sys}$ is the ionospheric delay after merging receiver and satellite pseudorange delays; u_r^s is the unit vector from receiver to satellite; Δr denotes the vector of the receiver position increment; $m_r^{s,Sys}$ is the mapping function of tropospheric zenith wet delay (ZWD) ZWD_r; $B_{r,f}^s = N_{r,f}^s + b_{r,f} - b_f^s$ is the un-differenced ambiguity; Sys represents the satellite system, including GPS, Galileo, and BDS; ISB^{Sys} represents the ISB parameters of Galileo and BDS relative to GPS; IFB^s is the IFB parameter of each GLONASS satellite relative to GPS.

For each epoch, the estimated parameters are,

$$X = (\Delta r^T, ZWD_r, d\bar{t}_r, (ISB^{Sys})^T, (IFB^s)^T, (\hat{I}_{r,1}^s)^T, (B_{r,1}^s)^T, (B_{r,2}^s)^T)^T \tag{4}$$

The extended Kalman filter is employed for the parameter estimation. Tropospheric ZWD ZWD_r and ionospheric slant delay $\hat{I}_{r,1}^s$ are estimated as random walk process noise of 1 × e-4 $m/\sqrt{s}$ and 3 $m/\sqrt{s}$, respectively. The receiver clock $d\bar{t}_r$ is estimated as epoch-wise white noise and the carrier phase ambiguity $B_r^s = N_f + b_{r,f} + b_f^s$, inter-system bias ISB^{Sys} and inter-frequency bias IFB^s parameters are estimated as constant values over time. ISB^{Sys} and IFB^s are applied for multi-GNSS and GLONASS frequency-division multiple access (FDMA) mode satellites, respectively.

Fixing the carrier phase ambiguity is not only essential to generate stable and high-precision atmospheric delay from all reference stations but also the key to realize rapid positioning on the users (Cui et al. 2021; Ge et al. 2007). UPD is used to implement integer-AR, where wide-lane (WL) ambiguity is fixed by rounding to the nearest integer, and narrow-lane (NL) ambiguity is solved using the least-squares ambiguity decorrelation adjustment (LAMBDA) method (Teunissen 1995). Once the AR is successfully performed on each reference station, the precise atmospheric delay can be derived and provided for modeling.

2.1. Tropospheric delay fitting model

The slant tropospheric delay consists of the dry and wet components, both of which could be expressed by

zenith delays with mapping functions (Boehm, Werl, and Schuh 2006; Böhm et al. 2014). The a priori zenith hydrostatic delay (ZHD) can be calculated using meteorological data and the Saastamoinen model (Saastamoinen 1972), and the ZWD is estimated as unknown parameter.

For the tropospheric delay modeling, the modified optimal fitting coefficients (MOFC) model is introduced to model the derived tropospheric ZWD (Cui et al. 2022):

$$\tilde{Z}_r = \left(a_0 + a_1 * d\varphi_i + a_2 * d\lambda_i + a_3 * d\varphi_i * d\lambda_i + a_4 * d\varphi_i^2 + a_5 * d\lambda_i^2\right) * e^{\left(\frac{dh_i}{a_H}\right)} \quad (5)$$

where the $a_0, a_1, a_2, a_3, a_4, a_5$ are the fitting coefficients of the model, the $e^{\left(\frac{dh_i}{a_H}\right)}$ refers to the altitude-related correction, and a_H is the scaling height, $d\varphi_i, d\lambda_i, dh_i$ are differences of latitude, longitude, and altitude between the users and reference stations.

2.2. Modified ionospheric delay fitting model

The ionospheric delay $I^s_{r,1}$ in Equation (4) includes the satellite and receiver differential code biases (DCBs). In large areas, satellite and receiver DCBs should be removed beforehand to maintain the "clean" ionospheric delay applied in modeling. The estimated ionospheric value can be expressed as,

$$\hat{I}^s_{r,1} = I^s_{r,1} + SPR = VTEC_r(d\varphi, d\lambda) * M(e) + SPR \quad (6)$$

where $M(e)$ is the ionospheric delay mapping function; $I^s_{r,1}$ is the "clean" slant ionospheric delay; The local ionospheric VTEC model on each station is introduced to model all satellite STEC and separate the satellite plus receiver (SPR) DCB biases from the ionospheric delays (Wang et al. 2020). After estimating and eliminating the SPRs, the satellite-wise STEC fitting model was built using all observed reference stations. Normally, a second-order polynomial model is applied for ionospheric delay modeling,

$$\tilde{I}^s_{r,1} = b_0 + b_1 * d\varphi_i + b_2 * d\lambda_i + b_3 * d\varphi_i * d\lambda_i + b_4 * d\varphi_i^2 + b_5 * d\lambda_i^2 \quad (7)$$

where $\tilde{I}^s_{r,1}$ is model fitted ionospheric delay, $b_0, b_1, b_2, b_3, b_4, b_5$ are the fitting coefficients of the model; $d\varphi_i$ and $d\lambda_i$ are differences of latitude and longitude between the reference point and ionospheric pierce points (IPPs), respectively.

Generally, a thin-layer assumption is introduced to model the ionospheric delay, usually referring to an altitude of 350 km, for all IPPs. Although the legacy polynomial model describes each satellite ionospheric slant delay on a thin-layer plane, it only achieves the mathematical fitting, which does not conform to the actual physical properties of the slant propagation path. We aim to achieve the fitting model in wide-area accelerating the PPP-RTK convergence. Due to a strong correlation between the magnitude of ionospheric delay and the lengths of propagation paths through the ionospheric regions, the modeling process should consider this correlation (Chen et al. 2022; Gu et al. 2022). Therefore, a new fitting model is introduced to consider the ionospheric slant delay propagation path properties in wide-area modeling. When constructing a high-precision model suitable for PPP-RTK in this paper, only the ionospheric slant delay estimated by the PPP-RTK server is needed, without any reliance on external information.

From Figure 1, the stations in the modeling areas receive the signal from a specific satellite. The satellite signals through the ionosphere start at about 1000 km and extend up to 50 km, i.e. the blue lines. We select a path at the center of coverage areas as the reference path (green line). The reference path is automatically selected according to the real-time modeled satellite coverage areas' IPPs latitude and longitude ranges. The differences between

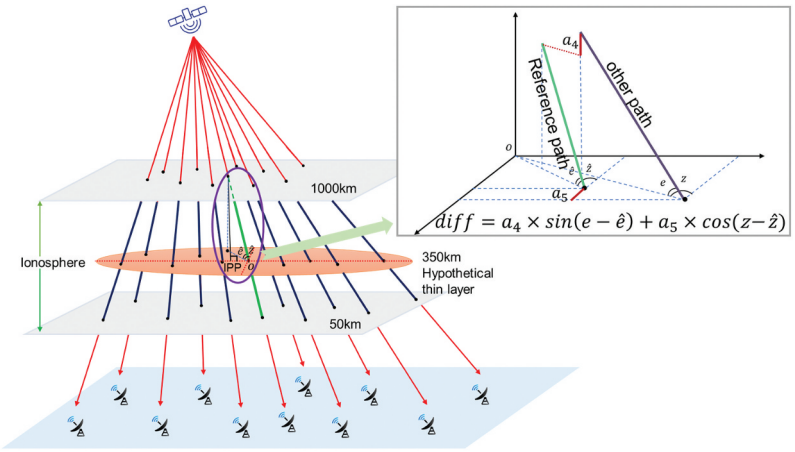

Figure 1. Illustration of ionospheric delay fitting model, blue lines are ionospheric delays for all stations and the green line is the reference propagation path.

all slant delays (blue line) and the reference delay (green line) can be calculated using trigonometric functions, with elevation and azimuth angle differences as inputs, i.e. the red line in the right-side figure.

$$\tilde{I}^s_{r,dif} = b_4 * \sin(e - \hat{e}) + b_5 * \cos(z - \hat{z}) \quad (8)$$

where $\tilde{I}^s_{r,dif}$ is the difference between the reference path and others; e and z are the elevation and azimuth angles of each station ionospheric delay, respectively; $\hat{e}$ and $\hat{z}$ are the elevation and azimuth angles of reference ionospheric delay, respectively.

In addition, the first-order polynomial model is provided as the basic model and the new ionospheric delay model $\tilde{I}^s_{r,m}$ can be presented as,

$$\tilde{I}^s_{r,m} = \underbrace{b_0 + b_1 * d\varphi_{ipp} + b_2 * d\lambda_{ipp} + b_3 * d\varphi_{ipp} * d\lambda_{ipp}}_{\tilde{I}^s_{r,1}} + \underbrace{b_4 * sin(e - \hat{e}) + b_5 * cos(z - \hat{z})}_{\tilde{I}^s_{r,dif}} \quad (9)$$

where $d\varphi_{ipp}$ and $d\lambda_{ipp}$ are the altitude and longitude coordinate differences between each ionospheric delay slant path IPP (blue line) and the reference path IPP (green line). The new model includes six model fitting coefficients $(b_0, b_1, \ldots, b_5)$ and the reference ionospheric delay IPP coordinates, and elevation and azimuth angles ($\hat{e}$ and $\hat{z}$). It should be noted that the model coefficients and reference path coordinates and angles are updated with real-time input IPPs.

The model is generated satellite-wise, whereby all satellite-specific slant delays are derived and collected for modeling. First, the reference ionospheric delay amongst all slant delays can be calculated in the modeling areas by determining the differences in latitude and longitude ranges. Therefore, the reference path IPP is also the nearest one to the center of coverage areas, and the reference coordinates, elevation, and azimuth angle can be determined. Subsequently, satellite-specific ionospheric delays from all stations can be introduced as input for the modeling, taking into account the differences in latitude, longitude, elevation angle, and azimuth angle with respect to the reference path. Finally, the iterative least-squares method is employed to solve the model coefficients.

In addition, the modeling precision is strongly related to data quality and sensitive to the outliers. For ionospheric delay modeling, the outlier detection is divided into two parts. Only stations with a fixing rate larger than 90% can be included in the modeling, and outliers larger than three times of the root mean squares (RMS) of modeling residuals will be down-weighted during processing iteration (Cui et al. 2022).

2.3. Atmosphere uncertainty information generation

Although the fitting model can correct a majority of the tropospheric and ionospheric delays, the unmodeled part remains on each reference station. Hence, the unmodeled residuals at these stations can be disseminated as,

$$I^s_r - \tilde{I}^s_r = \widehat{I^s_r}$$

$$Z_r - \tilde{Z}_r = \widehat{I^t_r} \quad (10)$$

where $\tilde{I}^s_r$ and $\tilde{Z}_r$, and $\widehat{I^s_r}$ and $\widehat{I^t_r}$ are ionospheric and tropospheric delay model fitted and unmodeled values, respectively.

To provide uncertainty information over wide-area, two sets of grids are generated relying on all reference station tropospheric ZWD and ionospheric delay fitting residuals. It should be noted that the interpolation accuracy will gradually decrease with the distance increasing. For precise generation of tropospheric delay uncertainty grid, the inverse distance weighting (IDW) interpolation method is employed, utilizing surrounding fitting residuals within a threshold range of 200 km. The threshold value exceeds the reference station spacing of 150 km and the extent of one degree of European latitude and longitude, which correspond to approximately 110 km and 60 km, respectively (Banville et al. 2022; Hirokawa, Fernández-Hernández, and Reynolds 2021).

$$l_{grid} = \sum\nolimits_{i=1}^{n} \widehat{l_i}(resi) \times \frac{w_i^s}{\sum_{i=1}^{n} w_i^s} \quad (11)$$

$$w_i^s = \frac{1}{d_i^{s2}} \tag{12}$$

where l_{grid} is the uncertainty grind point values; $\hat{l}_i(resi)$ is the fitting residuals of atmospheric delay; i.e. $\widehat{l_r^s}$ and $\widehat{l_r^t}$ for the ionospheric and tropospheric delays, respectively.

Unlike the tropospheric ZWD model, which is generated for all satellites and thus can directly apply the IDW method to calculate grid points for all satellites uncertainty, the ionospheric delay is modeled on a per-satellite basis. Therefore, different satellites exhibit varied modeling performances, i.e. the fitting residuals among different satellites are inconsistent. Fortunately, within local areas, the differences in residuals between different satellites are relatively small, typically within 4 cm. We organize all fitting residuals from smallest to largest for each grid point, considering a 150-km radius. The 90th percentile value, i.e. two times sigma value, is then selected as the uncertainty grid point.

The constraint value for the user can be determined by employing the IDW method with nearby points from the surrounding uncertainty grid. In areas with complete coverage, the user can utilize the surrounding four points for constraint determination. However, in boundary areas where coverage may be limited, the user can rely on three or two points. It should be noted that in the case of tropospheric ZWD, the interpolated uncertainty value is directly used as the constraint. To account for the differences in satellite modeling, the ionospheric uncertainty is combined with the modeling sigma to adjust the constraint according to the satellite-wise modeling performance, as shown in Equation (14).

$$l_{uncer} = \sum_{i=1}^{m} l_{grid} \times \hat{\sigma}_{sig}^s \times \frac{w_i^s}{\sum_{i=1}^{m} w_i^s} \tag{13}$$

$$\hat{\sigma}_{sig}^s = \sigma_{sig}^{s\,2} / \hat{\sigma}_{ave}, \hat{\sigma}_{ave} = \frac{\sum_j^n \sigma_{sig}^{s\,2}}{n} \tag{14}$$

where l_{uncer} is the interpolated uncertainty value; m is the total number of surrounding grid points used, with a maximum of 4 and a minimum of 1; σ_{sig}^s is the satellite-wise modeling sigma, which is the RMS of differences between model fitted values and PPP-AR derived values; $\hat{\sigma}_{sig}^s$ is the satellite-related factor for each satellite to adjust the uncertainty values from grid; $\hat{\sigma}_{ave}$ is the average value among all satellite modeling sigma; n is the satellite number applied in uncertainty calculation.

3. Experimental validations

In this section, the dataset and data processing strategy are described in detail.

3.1. Dataset

The EUREF Permanent GNSS Network (EPN) and its densification network are employed in the experiment. One hundred sixty-six stations, all of which include GPS/Galileo satellites, are used for atmospheric delay derivation and uncertainty grid generation, and the other 113 stations, which include GPS/Galileo/BDS/GLONASS satellites, are used for positioning verification. The GNSS observation data from the day of year (DOY) 270 to 300 in 2022 are used to perform the assessment. In addition, five days of observation data (DOY 58, 82, 83, 113, and 114, 2023) under active ionosphere conditions are also selected for modeling and positioning analysis as the ionosphere active conditions comparison group. Figure 2 presents the ionosphere *K*p index, which describes the activity of ionosphere. The *K*p index ranges from 0 to 3, indicating a calm ionosphere condition; from 3 to 6, indicating a moderate condition; and from 6 to 10, indicating an active condition. Generally, when the ionosphere *K*p index is larger than 6, it is usually associated with an ionosphere under active conditions.

From Figure 3, the uniformly distributed 166 reference stations marked as green dots with an average station-spacing of 150 km satisfying the requirement for the generation of 2°×2° grid points.

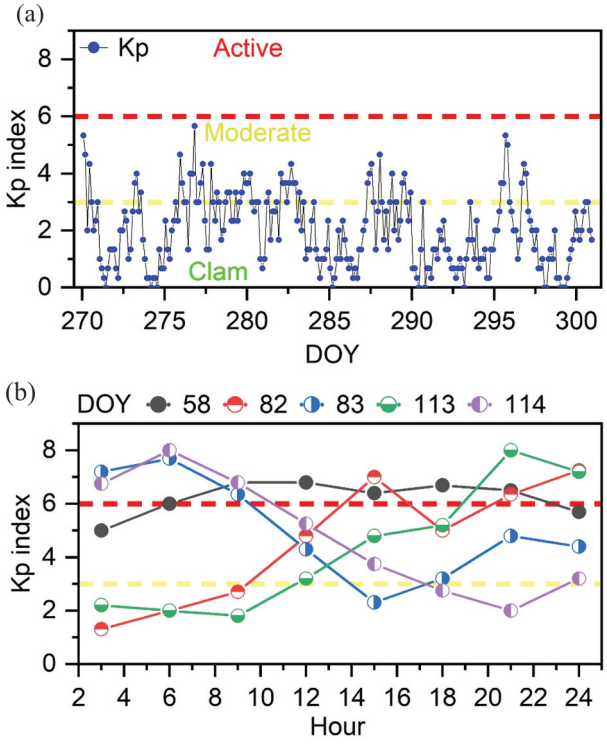

Figure 2. Ionosphere Kp index among all selected days. (a) Ionosphere *Kp* index from DOY 270 to 300, 2023; (b) Selected 5 days under ionospheric active conditions.

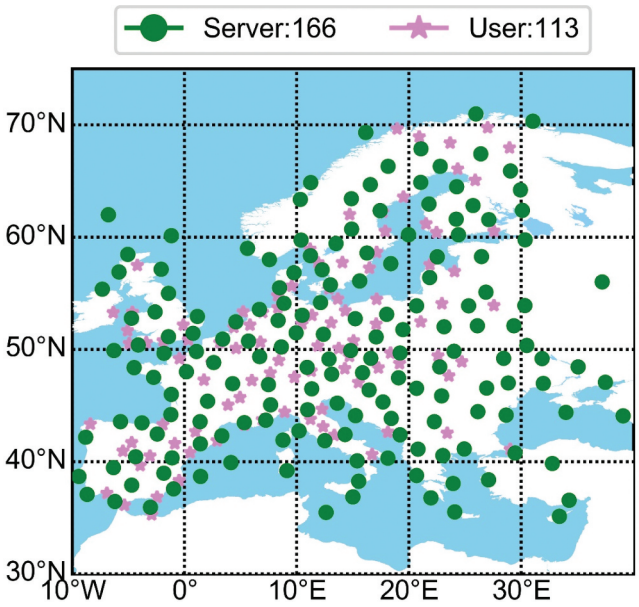

Figure 3. EPN stations and its densification network stations used for atmospheric delay derivation and precision grid map generation. One hundred sixty-six green dots (server) are reference stations and 113 purple stars (user) are positioning verification stations.

3.2. Data processing strategy

Data processing is divided into two parts: the server and the user. The main purpose of the server is to estimate and derive atmospheric delay for modeling. To guarantee the accuracy and stability of atmospheric parameters with continuous streams of data, we also perform the ambiguity resolution at each station on the server stations. The user employs the received model coefficients and uncertainty information to accelerate the ambiguity resolution and convergence. The procedure is shown in the flowchart of Figure 4.

Real-time stream multi-GNSS orbits and clocks with 5 s interval from GFZ are fixed in the processing. The precision of GFZ real-time products is evaluated by Li et al. (2022a), which is demonstrated to satisfy the requirements of real-time multi-GNSS high-precision data processing. Once the ambiguity resolution is successfully performed at all reference stations, the derived tropospheric and ionospheric delays can

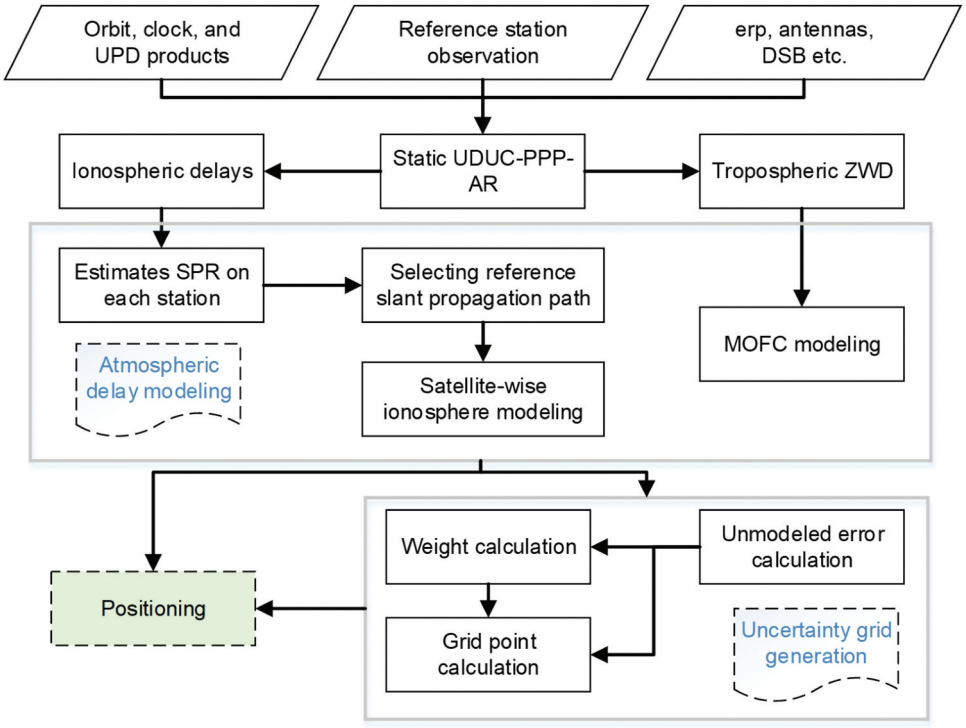

Figure 4. Flowchart of atmospheric delay modeling and positioning processing.

Table 1. PPP data processing strategies on service and user end.

Item	Service	User
System	GPS/Galileo	GPS/Galileo/GLONASS/BDS
Signal	GPS: L1+L2 GLONASS:G1+G2 Galileo:E1+E5a BDS:B1+B3	
Interval	30 s	
Cut-off elevation angle	7°	
Ambiguity fixing	WL: rounding; NL: LAMBDA searching, ratio-test with the threshold of 3	
Satellite orbit and clock	GFZ real-time products	
Satellite/receiver PCO/PCV	Igs20.atx	
Station displacement	Solid Earth tides, ocean tides, and pole tide displacements (IERS 2010)	
Phase wind-up	Corrected (Wu et al. 1993)	
Coordinates	Fixed	Estimated
Receiver clock offset	Estimated epoch-wisely, with the a priori values obtained from code-based positioning	
Slant ionospheric delay	Estimated	The augmentation information was used to provide the a priori value and the corresponding constraints is calculated from uncertainty grid
Troposphere estimation	The a priori ZHD from the Saastamoinen model with GPT2w meteorological data input, ZWD estimated with random walk process, GPT2w and VMF1 is used as the mapping function	The a priori delay and mapping function are the same as at the server, but the additional augmentation information was used to provide the a priori ZWD value and the corresponding constraints are calculated from uncertainty grid
Differential Code Biases	Corrected (Wang et al. 2015)	
Parameter estimator	Kalman filter	

Table 2. Four types of ionospheric delay model comparison.

Abbr.	Model	Coefficient number (X is number of satellites)
P1T0	First-order polynomial function	$4 \times X$
P2T0	Second-order polynomial function	$6 \times X$
P3T0	Third-order polynomial function	$11 \times X$
P1T1	First-order polynomial with sin and cos trigonometric functions	$6 \times X$ (coefficient) + $4 \times X$ (ref path)

be introduced for the modeling. Then, the unmodeled ZWD error at all reference stations and ionospheric delay on all IPPs are calculated separately and provided for uncertainty grid generation. Finally, the user uses real-time products and additional atmospheric delay fitting model coefficients and uncertainty information to perform positioning. The data processing strategy is described in Table 1.

In order to compare the performance of the proposed ionospheric delay model with legacy models, four schemes, listed in Table 2, will be performed and analyzed in the following sections. P and T separately denote the polynomial and trigonometric functions; X is the number of satellites. The numbers in polynomials denote the order level of the fitting model. In contrast, the 1 and 0 in trigonometric functions indicate whether they are enabled or not. The atmospheric delay modeling coefficient is calculated and updated every 30 s, and the uncertainty map is updated every 15 min.

4. Ionospheric delay model precision analysis

Using the received model fitting coefficients, the differences between PPP-derived and model-fitted values are calculated at all verification stations for all satellites during 30 days, and the results are presented in Figures 5 and 6 during test periods. It should be noted that the SPR biases are modeled and removed from the ionospheric delays in advance using the method proposed by Wang et al. (2015) and following the procedure of Cui et al. (2023).

For GPS satellites, the percentages of residuals less than 2.5 cm are 7.8%, 8.2%, 8.5%, and 18.5% for P1T0, P2T0, P3T0, and P1T1 models, respectively. As for Galileo, the corresponding numbers are 7.5%, 8.0%, 8.1%, and 16.6%. For residuals exceeding 10 cm, the percentages are as follows for GPS satellites: 70.4%, 69.2%, 68.5%, and 37.4% for P1T0, P2T0, P3T0, and P1T1 models, respectively. Correspondingly, Galileo satellites exhibit percentages of 71.2%, 70.5%, 69.9%, and 40.3%. Compared with the legacy polynomial fitting model, the proposed model significantly improves the modeling performance and reduces the number of larger residuals. Percentage of residuals smaller than 2.5 cm increases more than 10%, and residuals larger than 10 cm reduces more than 30%. This is mainly attributed to a more thorough consideration of the physical delay characteristics of the ionosphere during modeling, achieved by constructing the model based on the differences in path lengths between various paths. Additionally, the proposed model adopts a more rational adaptive approach to select the modeling range for each satellite. The reference satellite consistently resides at the center of the modeling region, and the size and location of the modeling area adjusts dynamically with changes in the satellite's trajectory.

We also calculate the average precision and standard deviation (STD) values derived from the absolute values of all residuals. In Figure 7, the GPS satellite average modeling precisions are 27.0 cm, 23.9 cm, 20.6 cm, and 9.7 cm for P1T0, P2T0, P3T0, and P1T1, respectively, and the precision for Galileo satellites are at a comparable level. The improvement

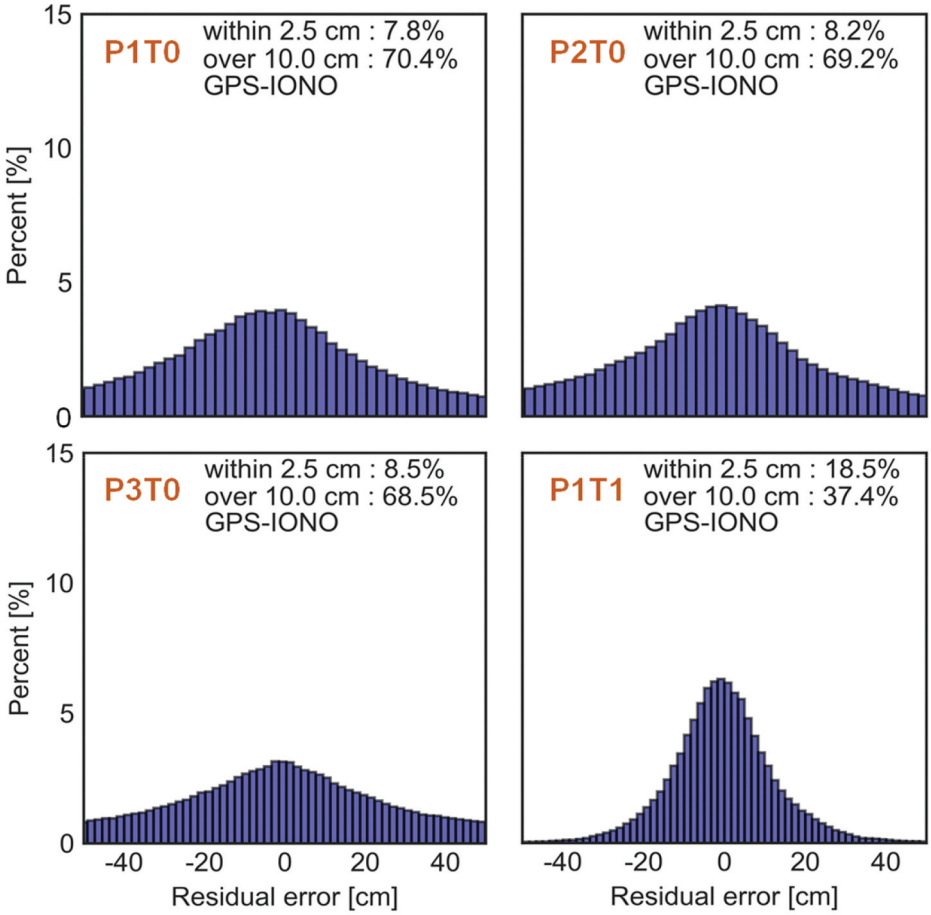

Figure 5. GPS satellites slant ionospheric delay differences between PPP-derived and model-fitted values on all reference stations.

precisions of the newly proposed model (P1T1) are 64.2%, 59.6%, and 53.0% compared to the polynomial functions with an order of one, two, and three, respectively. The modeling stability, which is presented by STD values, can also be improved by 56.1%, 52.3%, and 45.0%, respectively. The ionosphere fitting model can achieve an augmented precision of approximately 9.0 cm with fewer fitting coefficients in large areas with sparse station networks.

In addition, four model fitting performances are performed in active ionosphere conditions to verify the model performance in more active conditions as shown in Figure 8. The observations of five active days are used to perform four schemes, and the RMS of 24.3, 33.1, 41.4, and 47.9 cm are achieved for P1T1, P3T0, P2T0, and P1T0 schemes, respectively. Although the modeling precision is lower than that of calm and medium conditions, the proposed model consistently exhibits the superset fitting performance. Similar findings were reported by Zhu et al. (2022), who conducted modeling in the European region using 226 EPN stations. In active ionospheric conditions, their model achieved a TECU range of approximately 2.3 to 6 TECU (Zhu et al. 2022). In Australia, under active ionospheric conditions with Kp levels up to 6, an ionospheric model yielded values of up to 8 TECU, whereas for calm conditions, it was around 2.14 TECU (Liu et al. 2018). Even in interpolation mode, the RMS of post-fitting residuals could reach up to 2 TECU (Krypiak-Gregorczyk, Wielgosz, and Borkowski 2017). Typically, during active ionospheric or ionospheric scintillation periods, GNSS signals are significantly impacted, leading to a degradation in the performance of GNSS positioning. Consequently, maintaining satisfactory positioning accuracy is often challenging. Therefore, ionospheric models may also struggle to provide effective assistance for positioning during these periods (Hu et al. 2023).

5. Atmosphere uncertainty generation in large area

The modeling and uncertainty grid generation use the MOFC for tropospheric ZWD and proposed ionospheric slant delay fitting model, i.e. P1T1 scheme. Two 2° × 2° grid sets are provided separately for tropospheric ZWD and ionospheric slant ionospheric delays fitting models. The performance of modeling and corresponding uncertainty grids is assessed in the following.

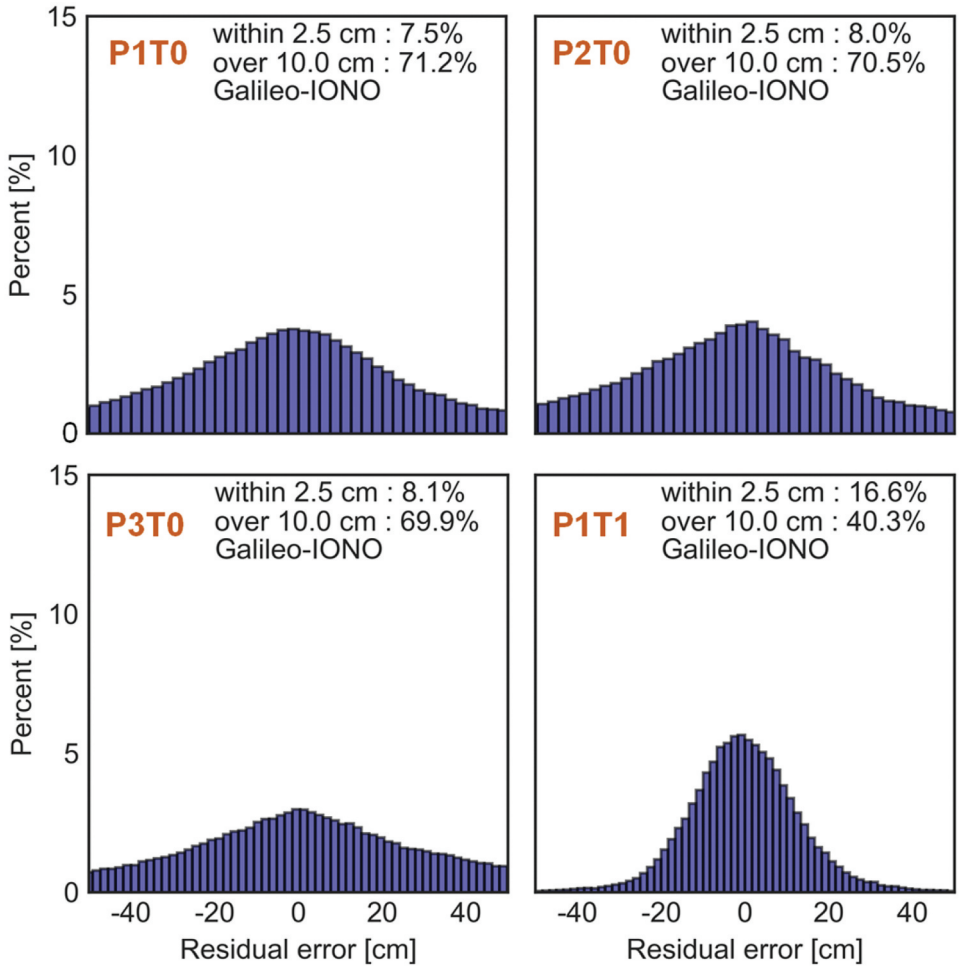

Figure 6. Galileo satellites slant ionospheric delay differences between PPP-derived and model-fitted values on all reference stations.

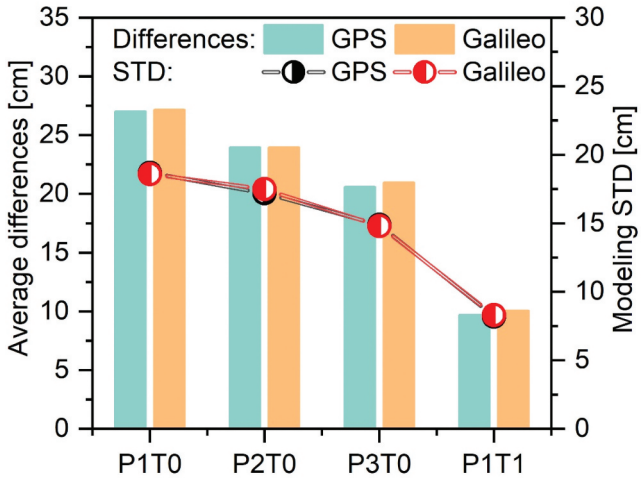

Figure 7. Average precision and STD value between PPP-derived and model-fitted differences for four schemes in 30 days. The absolute values are applied for calculation. Column bars and dots denote average value and modeling precision, respectively.

5.1. Troposphere model and uncertainty grid

We perform the tropospheric ZWD using all reference stations and analyze the modeling performance at all reference stations. The absolute differences between PPP-derived and model-fitted values at all stations are shown in Figure 9, and the corresponding uncertainty grid is shown in Figure 10.

The model can achieve an average accuracy of about 1.6 cm in the European region. While some

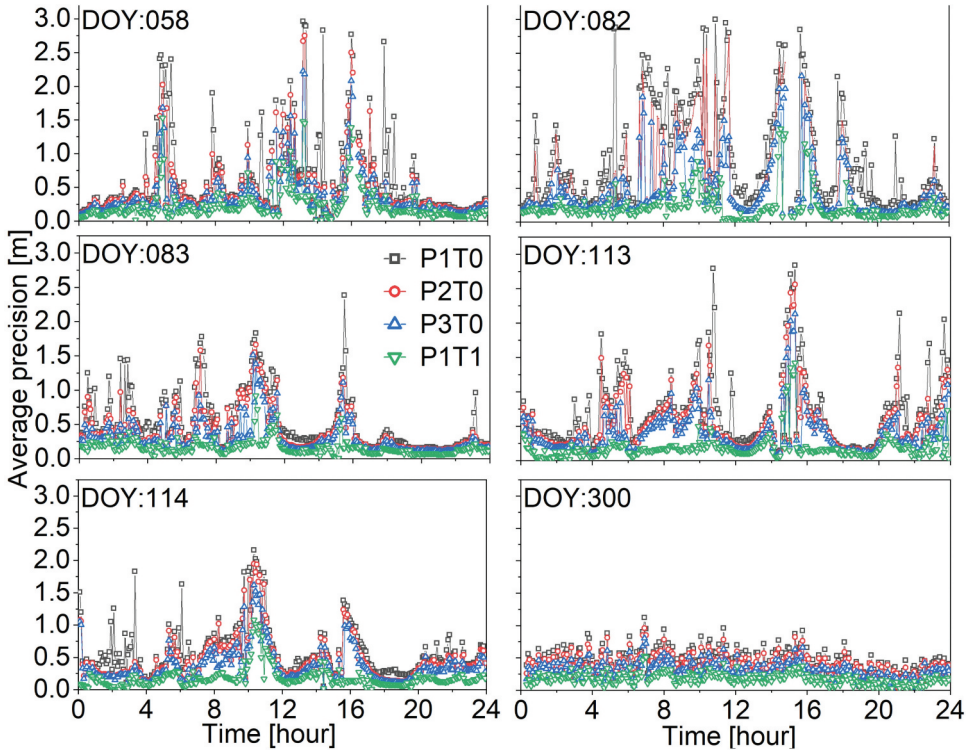

Figure 8. RMS of ionospheric delay modeling error in active/calm conditions for each epoch. The RMS is calculated using the difference between PPP-AR-derived and model-fitted values for every 5-min interval.

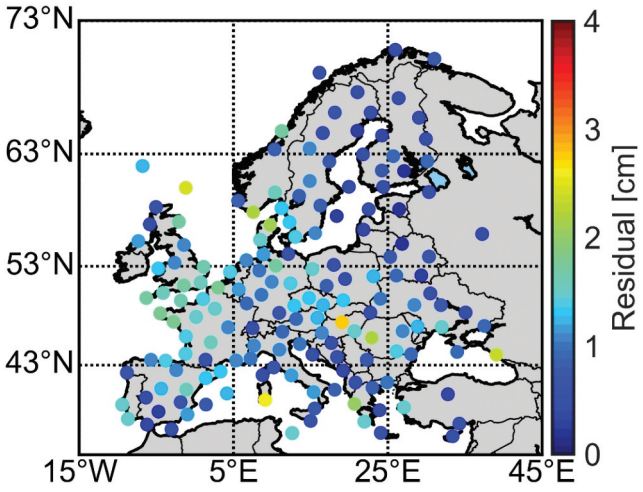

Figure 9. Tropospheric ZWD difference between PPP-derived and model-fitted values on all reference stations. Differences are calculated using 15-min data (14:00–14:15 DOY 270, 2022).

areas with high altitudes and border areas can reach up to 3.0 cm. Compared with the unmodeled residuals map (Figure 9), the uncertainty grid (Figure 10) shows a similar trend in each sub-grid area. This precision distribution is well represented in the tropospheric uncertainty by each grid point. Slight differences within 1 cm are achieved between the fitting residuals and the uncertainty grid.

5.2. Ionosphere model and uncertainty grid

The satellite-wise ionospheric slant delay fitting model differs from the tropospheric ZWD model. It provides a set of unmodeled residuals for each satellite. The differences between model-fitted and PPP-derived values for all GPS and Galileo satellites, as observed on all reference station's satellite IPPs between 14:00 and 14:15 on DOY 113, 2023, are presented in Figure 11, and the uncertainty grid is shown in Figure 12.

The average absolute difference of all satellite ionospheric slant delays is 11.3 cm. The fitting model uses the ionospheric delay after removing the SPRs for all satellites. Therefore, the precision of ionospheric delay is mainly impacted by the latitudinal and meteorological variations. Although each satellite has different coverage areas, slight differences within 4.3 cm are achieved in the overlapping areas. We arrange all

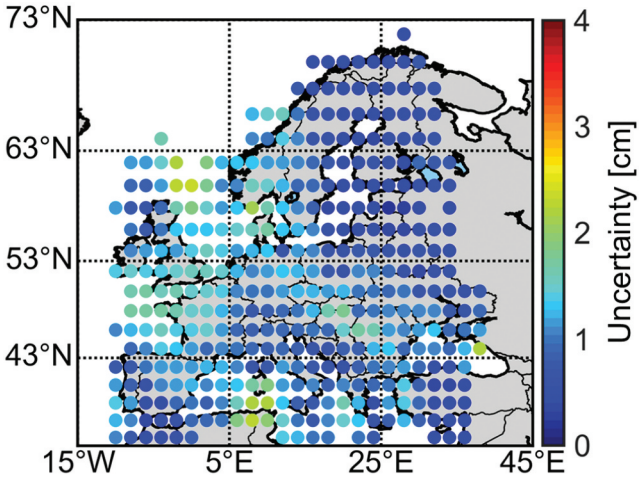

Figure 10. Tropospheric ZWD uncertainty grid. Uncertainty points are calculated from ZWD differences between model fitted values and PPP-AR-derived values using 15-min (14:00–14:15) DOY 270, 2022.

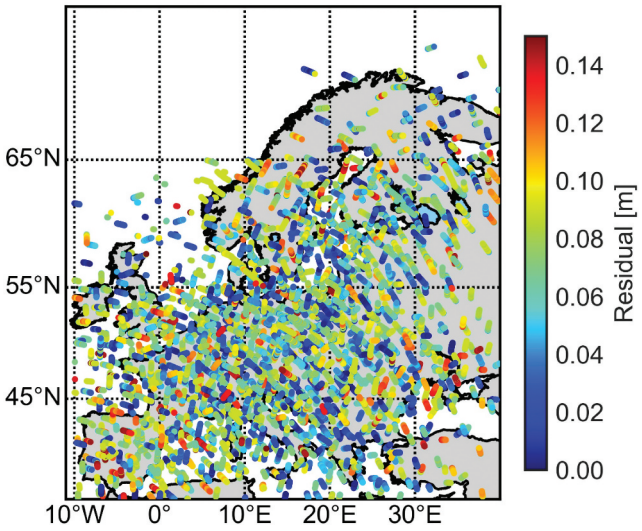

Figure 11. Satellite-wise differences of slant ionospheric delay between modeled values and PPP-AR-derived values for all selected reference stations at 14:00–14:15 on DOY 113, 2023.

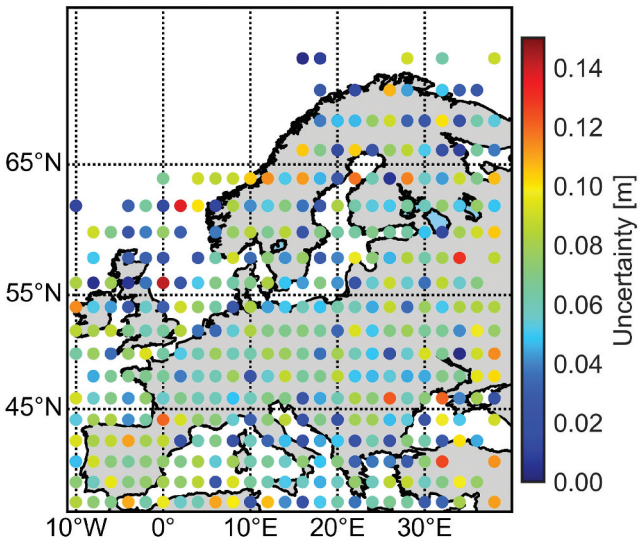

Figure 12. Large-area satellite-wise slant ionospheric delay fitting model uncertainty using 1-min pieces basis between modeled and PPP-AR-derived values between 14:00–14:15 on DOY 113, 2023.

satellite fitting residuals in ascending order, and then select the 90th percentile value as the grid point value. To minimize data transmission, a single accuracy map is employed to represent uncertainty in both the troposphere and ionosphere. Different from the troposphere, ionospheric uncertainty grid points are derived from the fitting residuals of multiple satellites. The 90th percentile of residuals from all satellites, sorted in ascending order around each grid point, is selected as its representative value. This approach effectively filters out extreme fitting residuals while maintaining a reasonable and lenient standard for the majority of satellite data. The use of one map for all satellites is intended to meet the communication requirements and reduce the volume of data transmission. In addition, to adjust the constraint for each satellite based on the uncertainty grid, a factor derived from the satellite-wise modeling sigma is applied to recalculate the value as the constraint. Therefore, this chosen value is suitable for all satellites and avoids creating overly restrictive or wrong constraints. When compared to the unmodeled residuals in Figure 11, the grid points exhibit closer performance and distribution. Additionally, the satellite-wise weight is introduced into the user-end utilization to decrease the impact caused by the difference among modeling for each satellite, thus allowing for generating a common grid for all satellites in wide-area. Therefore, one set of grid models is sufficient to represent the performance of satellite-wise ionospheric delay fitting model.

The fitting model coefficients can be broadcast via satellite communication, providing augmentation services with low communication volume in wide-area at any time. Conducting the modeling, the modeled ionospheric and tropospheric corrections can serve as essential information. In the figure above, the grid is 2°×2° with an inter-station distance of 110 km and maximum of 475 grids serves for the uncertainty grid in European.

6. Positioning performance verification

In positioning, we conduct separate comparisons between the newly proposed ionospheric delay fitting model and the legacy models. Additionally, we compare the positioning performance by applying different modeling precision and automatic calculation using uncertainty grids. For convergence analysis, the daily observations are divided into 24 one-h sub-sessions, resulting in a total of 94,920 sub-sessions over all days. Because the positioning initial is reset every hour, the positioning performance could be affected when the ionosphere and troposphere are under more active conditions and would be reflected in the convergence time. The results are obtained by considering the 90th percentile of all absolute positioning errors for each processing epoch. The average positioning result denotes the overall atmosphere performance, including active and calm conditions, and the 90th percentile result can present the positioning result at more active or worse modeling states. Coordinate biases are determined by comparing the estimated positions to the coordinates obtained from static solutions. Convergence is defined as the time required to achieve a positioning error of less than 10 cm and maintain it for at least ten epochs. For ambiguity resolution validation, UPD is used to implement integer-AR, where WL ambiguity is fixed by rounding to the nearest integer, and NL ambiguity is solved using the LAMBDA method. The WL ambiguity resolution is validated by the fixing probability given by (Dong and Bock 1989) while the NL by the ratio-test with the threshold of 3 (Verhagen and Teunissen 2012).

6.1. Different ionosphere models positioning performance

To compare and analyze the performance of the proposed ionospheric delay fitting model in positioning, Figure 13 and Table 3 present the kinematic single-epoch results for the horizontal (H) and vertical (V) components of user's position in six schemes. These schemes are abbreviated as PPP, PPP-AR, P1T0, P2T0, P3T0, and P1T1. The PPP and PPP-AR schemes do not utilize any external atmospheric augmentation. In all augmentation solutions, i.e. P1T0, P2T0, P3T0, and P1T1, the consistent tropospheric ZWD MOFC model is applied. The PPP solution represents only the float solution, while integer ambiguities are resolved in other five schemes. In this section, the ionospheric delay is modeled using different fitting models. Consequently, the three-time modeling sigma derived from the respective model is applied as the constraint. Further details regarding the data processing strategies can be found in Table 1.

From Figure 13, the PPP scheme takes the longest convergence time, reaching up to 13.0 and 17.0 min for horizontal and vertical components, respectively. The PPP-AR scheme can reach convergence times of 11.5 and 16.5 min with the aid of ambiguity resolution. On the other hand, by introducing the ionospheric corrections and the tropospheric ZWD, the convergence can be significantly accelerated. The legacy polynomial fitting model, P1T0, P2T0, and P3T0 schemes can achieve 9.5, 8.0, and 7.5 min for horizontal components and 14.5, 13.5, and 11.5 min for vertical components, respectively. Compared with the traditional model, P1T1 scheme significantly improves the performance to 5.0 and 7.0 min for horizontal and vertical components, respectively. The proposed model achieves improvements on average convergence time of 44.3%, 39.1%, and 35.0% in horizontal and 45.5%, 36.5%, and 21.7% in vertical with

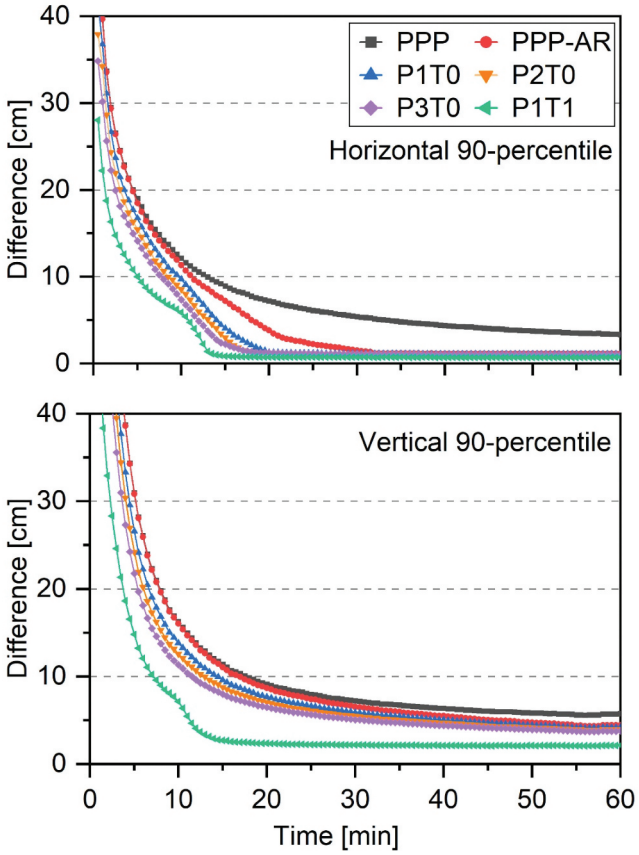

Figure 13. The time series of the 90th percentile of horizontal (top) and vertical (bottom) positioning error of six groups of multi-GNSS PPP solutions.

Table 3. The positioning result of average and 90th percentiles convergence time for six schemes.

	Average value/min		90th percentile/min	
Scheme	H	V	H	V
PPP	8.6	13.4	13.0	17.0
PPP-AR	7.9	10.9	11.5	16.5
P1T0	7.0	9.9	9.5	14.5
P2T0	6.4	8.5	8.0	13.5
P3T0	6.0	6.9	7.5	11.5
P1T1	**3.9**	**5.4**	**5.0**	**7.0**

respect to P1T0, P2T0, and P3T0 schemes, respectively. For the positioning results using different types of ionosphere products, the ambiguity fixing rate of PPP-AR is only 91%, and its first fixing time requires 13 min as well. With the intervention of different types of ionosphere model information, the ambiguity fixing time speeds up. The 90th percentile fixing time of P1T0, P2T0, P3T0, and P1T1 results requires 11.5, 10.0, 8.5, and 6.0 min, respectively, and the fixing rates are 92.3%, 93.7%, 94.6%, and 95.9%, respectively.

6.2. Positioning performance between different constraints

However, even though the proposed model can achieve a better performance than other schemes, the value of the constraints is obtained from the modeling accuracy, which is difficult to express the correction performance in the coverage areas well. Therefore, the uncertainty grid is introduced and compared with modeling precision constraints. Positioning with kinematic solution on all verification stations is implemented with four ionosphere weighting strategies: the fixed RMS value of one-time-sigma, i.e. Sigma-1, three-time-sigma, i.e. Sigma-3, and five-time-sigma, i.e. Sigma-5, and the automatically calculated value from the uncertainty grid, i.e. Grid (auto-adjustment). Here the adjusted sigma refers to $\hat{\sigma}^s_{sig}$ while the others refer to σ^s_{sig} in Equation (14). In addition, we present the constraint value on the OROS station as an example in Figure 14 to compare the constraints from each scheme and residuals between PPP-derived and model-fitted. It should be noted that the "Resi" value (shown in Figure 14) of IONO is the average difference between model fitting and PPP-derived of all IPPs. The difference between "Resi" and "Grid" is usually less than 3 cm, confirming the precision of uncertainty grid generation. Additionally, to prevent occasional instances of excessively small differences in residual calculations, we establish minimum thresholds for the uncertainties in the ionosphere and troposphere, set at 3 cm and 3 mm, respectively. When the difference is less than these thresholds, the uncertainty grid information is constrained to the minimum threshold values. Finally, all solutions are performed and presented in Figure 15 and Table 4.

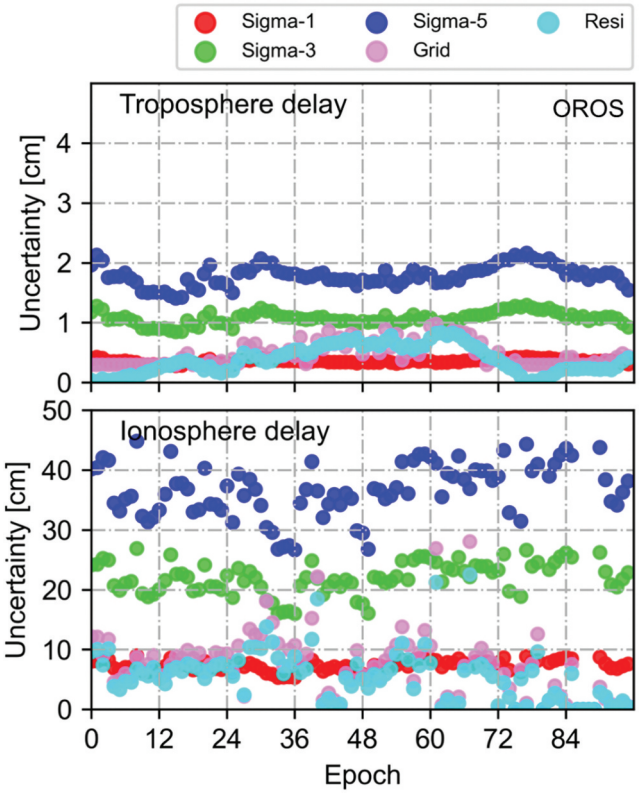

Figure 14. Uncertainty information at OROS station using modeling sigma and grid calculation, and the residuals between PPP-derived and model-fitted set as references. Top and bottom panels are troposphere and ionosphere uncertainty values, respectively.

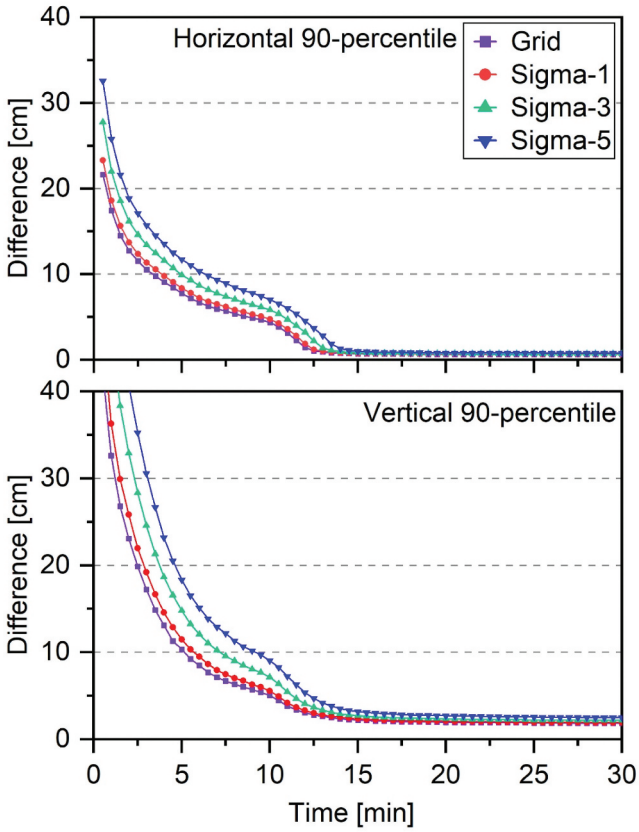

Figure 15. The time series of the 90th percentile of horizontal (top) and vertical (bottom) positioning error of four groups solutions.

Table 4. Positioning result of average and 90th percentiles convergence time for different constraint implementation.

	Average value/min		90th percentile/min	
Mode	H	V	H	V
Sigma-1	3.3	4.9	3.5	6.5
Sigma-3	3.9	5.4	5.0	7.0
Sigma-5	4.9	6.8	7.0	9.0
Grid	**2.3**	**3.8**	**3.0**	**5.0**

Table 5. Positioning result of average convergence time for ionosphere active and clam conditions.

	Clam/min		Active/min	
Mode	H	V	H	V
Sigma-1	3.1	4.7	4.2	5.8
Sigma-3	3.8	5.2	4.3	6.3
Sigma-5	4.7	6.4	5.8	8.5
Grid	**2.2**	**3.7**	**2.7**	**4.2**

Among all the schemes, the Grid scheme demonstrates the best performance by adaptively determining the atmosphere constraints based on the uncertainty grids. The Sigma-1 scheme significantly improves the performance compared to the Sigma-3 and Sigma-5 schemes. It is worth noting that, while the constraint value of Sigma-1 for ionospheric error may be over-optimistic during certain periods, as indicated in the ionosphere precision results in Figure 14, the Sigma-3 and Sigma-5 schemes provide more conservative constraints for ionospheric delay correction. As shown in Figure 15, the Grid scheme reduces the convergence time in horizontal and vertical components from 5.0 and 7.0 min in the Sigma-3 scheme to 3.0 and 5.0 min, respectively. Furthermore, the auto-adjustment Grid scheme not only reduces the convergence time but also significantly improves the positioning precision. Furthermore, when different types of constraints are used, there are also differences in ambiguity fixing with the change of convergence speed. Among them, Sigma-1, Sigma-3, and Sigma-5 achieved ambiguity fixing rates of 96.2%, 95.9%, and 94.1%, respectively. In contrast, the Grid scheme provide a fixing rate of up to 96.7%. Moreover, the first time to fixing based on the proposed model was improved from 6.0 min of Sigma-3 to 5.0 min.

In addition, in Table 4, the Grid scheme demonstrates average improvements of 30.3%, 41.0%, and 53.1% for the horizontal component, and 22.4%, 29.6%, and 44.1% for the vertical component, with respect to the Sigma-1, Sigma-3, and Sigma-5 schemes, respectively. Furthermore, the introduction of uncertainty grids leads to a significant reduction in average convergence time to 2.3 and 3.8 min for horizontal and vertical components, respectively. For the average result, the GPS+Galileo PPP-RTK achieves 2.5 and 4.2 min for horizontal and vertical components, respectively, slightly increasing than all constellation solutions. These results highlight the advantage of the Grid solution over the Sigma-1, Sigma-3, and Sigma-5 schemes, indicating the importance of proper constraints for ionosphere corrections. By applying proper tropospheric and ionospheric constraints, the user's estimation of ZWD and ionospheric delay parameters can achieve a higher level of accuracy faster while reducing their correlations with other parameters. The iteratively extended Kalman filter effectively adjusts the variance of ionospheric and tropospheric delay constraints. Overall, the generated uncertainty grids automatically determine the appropriate constraints, resulting in accelerated convergence.

In Table 5, we present the results that include both the active and calm periods of the ionosphere. To further compare the positioning performance under different degrees of ionosphere activity, we, respectively, present the positioning results as shown in Table 5. The comparison experiment is conducted on 5 days with active ionosphere conditions and 30 calm days. The average convergence time is 2.2 and 2.7 min for the horizontal component and 3.7 and 4.2 min for the vertical component, respectively. The relatively active ionosphere has a certain influence on the results of PPP-RTK, thus resulting in a slower convergence.

7. Conclusions

This work presents an effective model for ionospheric slant delay that considers the differences between the auto-selected optimum reference propagation path and other paths in coverage areas. Additionally, uncertainty grids of the troposphere and ionosphere are generated using the corresponding fitting models. By utilizing this model and the associated uncertainty information, fast PPP ambiguity resolution can be achieved over wide-area with less correction model coefficients.

This method is validated with observation data from the EPN stations. PPP-AR is performed at the reference stations using a multi-GNSS real-time product stream, and regional atmospheric corrections are derived for modeling purposes. The proposed ionospheric delay model takes into account the differences in the slant propagation path between the reference path and others to accurately capture the physical characteristics of the ionospheric delay. Compared with the legacy polynomial fitting model, the proposed model demonstrates significant improvements in modeling performance and a reduction in the number of larger residuals. Specifically, residuals smaller than 2.5 cm show an improvement of more than 10%, while residuals larger than 10 cm exhibit a reduction of more than 30%. The average ionospheric delay modeling precision is improved by up to 60% in European region with six coefficients and four reference path information. The accuracy of the tropospheric modeling achieves about 1.6 cm with seven coefficients. In

addition, two sets of 2°×2° uncertainty grids are introduced based on the unmodeled errors between PPP-AR-derived and model-fitted values from all reference stations. These atmospheric grids effectively describe the unmodeled atmospheric residual errors within each sub-region.

With the proposed ionosphere model and tropospheric MOFC model, positioning convergence can be achieved in 3.9 and 5.4 min for the horizontal and vertical components, respectively. These convergence times represent a significant reduction compared to the legacy polynomial fitting models. The average convergence time is improved by 44.3%, 39.1%, and 35.0% for horizontal component, and 45.5%, 36.5%, and 21.7% for vertical component, with respect to first-, second-, and third-order polynomial fitting model schemes, respectively. In addition, the uncertainty grid provides valuable assistance, resulting in an improvement of 42.1% and 28.8% when compared to the scheme applying the three-time modeling precision constraint. Convergence can be achieved in 2.3 and 3.8 min for horizontal and vertical components, respectively. The atmosphere uncertainty grid, based on the fitting model, effectively presents the real-time modeling accuracy of tropospheric and ionospheric corrections over large areas with sparse resolution.

Acknowledgments

The authors are grateful to the EPN for providing open GNSS data. Also, the authors would like to thank GFZ for providing ionosphere *Kp* index.

Disclosure statement

No potential conflict of interest was reported by the author(s).

Funding

This research is supported by the National Natural Science Foundation of China [grant numbers 42404027, 42374026], Fundamental Research Funds for the Central Universities [grant numbers 300102264105, 300102263401], National Key R&D Program of China [grant numbers 2023YFC3008300, 2023YFC3008304], and China Postdoctoral Science Foundation [No. 2024M762766].

Notes on contributors

Bobin Cui is a lecturer at Chang'an University, China. He received his PhD degree from Technische Universität Berlin, Germany. His research interests are global navigation satellite systems, PPP-RTK and atmosphere modeling.

Jungang Wang is a research scientist at the GFZ section of Space Geodetic Techniques. He received his PhD degree from Technische Universität Berlin, Germany. His research interests are atmospheric effects in space geodesy, global navigation satellite systems, very long baseline interferometry, satellite laser ranging, and multi-technique integrated processing.

Pan Li is a professor at Chang'an University, China. He obtained his Ph.D. from Wuhan University, China. His current research focuses mainly on GNSS precise point positioning and ambiguity resolution.

Jiahuan Hu received his PhD degree from York University, Canada. His main research interest is multi-GNSS precise point positioning ambiguity resolution and smartphone positioning.

Xiang Zuo is a Ph.D. student at the Technische Universität Berlin, Germany. His current research is multi-GNSS real-time clock estimation and positioning.

Longjiang Tang is a Ph.D. student at the Technische Universität Berlin and GFZ German Research Centre for Geosciences. His current research is multi-GNSS real-time orbit determination.

Authors contribution

BC initiated the study, BC and PL developed the software for analysis, BC analyzed the data, BC and JW wrote the manuscript. All authors provided critical feedback and reviewed the paper.

Availability of data and material

The orbit and clock product we used is 139.17.3.115:2101/SSRA00GFZ0. The GNSS data provided by the EPN can be accessed from https://epncb.eu/ftp/obs/. The ionosphere Kp index can be found from https://kp.gfz-potsdam.de/en/hp30-hp60/.

ORCID

Bobin Cui http://orcid.org/0000-0003-3229-7657
Jungang Wang http://orcid.org/0000-0002-7060-5342
Pan Li http://orcid.org/0000-0002-1358-4119
Jiahuan Hu http://orcid.org/0000-0001-9094-2859
Xiang Zuo http://orcid.org/0000-0003-0215-2131
Longjiang Tang http://orcid.org/0000-0002-6453-2546

References

Banville, S., E. Hassen, M. Walker, and J. Bond. 2022. "Wide-Area Grid-Based Slant Ionospheric Delay Corrections for Precise Point Positioning." *Remote Sensing* 14 (5): 1073. https://doi.org/10.3390/rs14051073.

Bilitza, D. 2018. "IRI the International Standard for the Ionosphere." *Advances in Radio Science* 16:1–11. https://doi.org/10.5194/ars-16-1-2018.

Boehm, J., B. Werl, and H. Schuh. 2006. "Troposphere Mapping Functions for GPS and Very Long Baseline Interferometry from European Centre for Medium-Range Weather Forecasts Operational Analysis Data." *Journal of Geophysical Research Solid Earth* 111 (B2). https://doi.org/10.1029/2005jb003629.

Böhm, J., G. Möller, M. Schindelegger, G. Pain, and R. Weber. 2014. "Development of an Improved Empirical Model for Slant Delays in the Troposphere (Gpt2w)." *GPS Solutions* 19 (3): 433–441. https://doi.org/10.1007/s10291-014-0403-7.

Boisits, J., M. Glaner, and R. Weber. 2020. "Regiomontan: A Regional High Precision Ionosphere Delay Model and Its Application in Precise Point Positioning." *Sensors (Basel)* 20 (10). https://doi.org/10.3390/s20102845.

Cabinet Office. 2020. "Quasi-Zenith Satellite System Performance Standard." PSQZSS–002. https://qzss.go.jp/en/technical/ps-is-qzss/ps-is-qzss.html.

Chen, J., X. Ren, S. Xiong, and X. Zhang. 2022. "Modeling and Analysis of an Ionospheric Mapping Function Considering Azimuth Angle: A Preliminary Result." *Advances in Space Research* 70 (10): 2867–2877. https://doi.org/10.1016/j.asr.2022.07.041.

Cui, B., X. Jiang, J. Wang, P. Li, M. Ge, and H. Schuh. 2023. "A New Large-Area Hierarchical PPP-RTK Service Strategy." *GPS Solutions* 27 (3): 134. https://doi.org/10.1007/s10291-023-01476-8.

Cui, B., P. Li, J. Wang, M. Ge, and H. Schuh. 2021. "Calibrating Receiver-Type-Dependent Wide-Lane Uncalibrated Phase Delay Biases for PPP Integer Ambiguity Resolution." *Journal of Geodesy* 95 (7). https://doi.org/10.1007/s00190-021-01524-6.

Cui, B., J. Wang, P. Li, M. Ge, and H. Schuh. 2022. "Modeling Wide-Area Tropospheric Delay Corrections for Fast PPP Ambiguity Resolution." *GPS Solutions* 26 (2). https://doi.org/10.1007/s10291-022-01243-1.

Dong, D.-N., and Y. Bock. 1989. "Global Positioning System Network Analysis with Phase Ambiguity Resolution Applied to Crustal Deformation Studies in California." *Journal of Geophysical Research Solid Earth* 94 (B4): 3949–3966. https://doi.org/10.1029/JB094iB04p03949.

Ge, H., B. Li, S. Jia, L. Nie, T. Wu, Z. Yang, J. Shang, Y. Zheng, and M. Ge. 2021. "LEO Enhanced Global Navigation Satellite System (LeGNSS): Progress, Opportunities, and Challenges." *Geo-Spatial Information Science* 25 (1): 1–13. https://doi.org/10.1080/10095020.2021.1978277.

Ge, M., G. Gendt, M. Rothacher, C. Shi, and J. Liu. 2007. "Resolution of GPS Carrier-Phase Ambiguities in Precise Point Positioning (PPP) with Daily Observations." *Journal of Geodesy* 82 (7): 389–399. https://doi.org/10.1007/s00190-007-0187-4.

Gu, S., C. Gan, C. He, H. Lyu, M. Hernandez-Pajares, Y. Lou, J. Geng, and Q. Zhao. 2022. "Quasi-4-Dimension Ionospheric Modeling and Its Application in PPP." *Satellite Navigation* 3 (1). https://doi.org/10.1186/s43020-022-00085-z.

Hernández-Pajares, M., D. Roma-Dollase, A. Krankowski, A. García-Rigo, and R. Orús-Pérez. 2017. "Methodology and Consistency of Slant and Vertical Assessments for Ionospheric Electron Content Models." *Journal of Geodesy* 91 (12): 1405–1414. https://doi.org/10.1007/s00190-017-1032-z.

Hirokawa, R., I. Fernández-Hernández, and S. Reynolds. 2021. "PPP/PPP-RTK Open Formats: Overview, Comparison, and Proposal for an Interoperable Message." *Navigation* 68 (4): 759–778. https://doi.org/10.1002/navi.452.

Hobiger, T., R. Ichikawa, Y. Koyama, and T. Kondo. 2008. "Fast and Accurate Ray-Tracing Algorithms for Real-Time Space Geodetic Applications Using Numerical Weather Models." *Journal of Geophysical Research: Atmosphere* 113 (D20302). https://doi.org/10.1029/2008JD010503.

Hu, J., B. Cui, P. Li, S. Bisnath, and K. Zheng. 2023. "Exploring the Role of PPP–RTK Network Configuration: A Balance of Server Budget and User Performance." *GPS Solutions* 27 (4). https://doi.org/10.1007/s10291-023-01518-1.

IERS Conventions. 2010. *IERS Technical Note*, In edited by G. Petit and B. Luzum, 179. Vol. 36. Frankfurt am Main: Verlag des Bundesamts für Kartographie und Geodäsie.

Ji, R., X. Jiang, X. Chen, H. Zhu, M. Ge, and F. Neitzel. 2022. "Quality Monitoring of Real-Time GNSS Precise Positioning Service System." *Geo-Spatial Information Science* 26 (1): 1–15. https://doi.org/10.1080/10095020.2022.2070554.

Krypiak-Gregorczyk, A., P. Wielgosz, and A. Borkowski. 2017. "Ionosphere Model for European Region Based on Multi-GNSS Data and TPS Interpolation." *Remote Sensing* 9 (12): 1221. https://doi.org/10.3390/rs9121221.

Li, B., H. Ge, Y. Bu, Y. Zheng, and L. Yuan. 2022a. "Comprehensive Assessment of Real-Time Precise Products from IGS Analysis Centers." *Satellite Navigation* 3 (1). https://doi.org/10.1186/s43020-022-00074-2.

Li, P., B. Cui, J. Hu, X. Liu, X. Zhang, M. Ge, and H. Schuh. 2022b. "PPP-RTK Considering the Ionosphere Uncertainty with Cross-Validation." *Satellite Navigation* 3 (1). https://doi.org/10.1186/s43020-022-00071-5.

Li, X., J. Huang, X. Li, H. Lyu, B. Wang, Y. Xiong, and W. Xie. 2021. "Multi-Constellation GNSS PPP Instantaneous Ambiguity Resolution with Precise Atmospheric Corrections Augmentation." *GPS Solutions* 25 (3). https://doi.org/10.1007/s10291-021-01123-0.

Li, X., X. Zhang, and M. Ge. 2011. "Regional Reference Network Augmented Precise Point Positioning for Instantaneous Ambiguity Resolution." *Journal of Geodesy* 85 (3): 151–158. https://doi.org/10.1007/s00190-010-0424-0.

Liu, J., R. Chen, Z. Wang, and H. Zhang. 2010. "Spherical Cap Harmonic Model for Mapping and Predicting Regional TEC." *GPS Solutions* 15 (2): 109–119. https://doi.org/10.1007/s10291-010-0174-8.

Liu, Q., M. Hernández-Pajares, H. Yang, E. Monte-Moreno, D. Roma-Dollase, A. García-Rigo, Z. Li, et al. 2021. "The Cooperative IGS RT-GIMs: A Reliable Estimation of the Global Ionospheric Electron Content Distribution in Real Time." *Earth System Science Data* 13 (9): 4567–4582. https://doi.org/10.5194/essd-13-4567-2021.

Liu, T., B. Zhang, Y. Yuan, and M. Li. 2018. "Real-Time Precise Point Positioning (RTPPP) with Raw Observations and Its Application in Real-Time Regional Ionospheric VTEC Modeling." *Journal of Geodesy* 92 (11): 1267–1283. https://doi.org/10.1007/s00190-018-1118-2.

Lu, C., X. Li, F. Zus, R. Heinkelmann, G. Dick, M. Ge, J. Wickert, and H. Schuh. 2017. "Improving BeiDou Real-Time Precise Point Positioning with Numerical Weather Models." *Journal of Geodesy* 91 (9): 1019–1029. https://doi.org/10.1007/s00190-017-1005-2.

Lyu, S., Y. Xiang, B. Soja, N. Wang, W. Yu, and T.-K. Truong. 2023. "Uncertainties of Interpolating Satellite-Specific Slant Ionospheric Delays and Impacts on PPP-RTK." *IEEE Transactions on Aerospace and Electronic Systems* 60 (1): 490–505. https://doi.org/10.1109/TAES.2023.3332565.

Lyu, S., Y. Xiang, Y. Zhang, H. Yang, L. Pei, W. Yu, and T.-K. Turong. 2023. "A Consistent and Grid-Based Regional Slant Ionospheric Model with an Increasing Number of Satellite Corrections for PPP-RTK." *GPS Solutions* 27 (3). https://doi.org/10.1007/s10291-023-01439-z.

Manzoni, M., N. Petrushevsky, C. Wu, S. Tebaldini, A. V. Monti-Guarnieri, and M. Liao. 2024. "SAR

Sensing of the Atmosphere: Stack-Based Processing for Tropospheric and Ionospheric Phase Retrieval." *Geo-Spatial Information Science* 27 (3): 624–637. https://doi.org/10.1080/10095020.2024.2330556.

Nadarajah, N., A. Khodabandeh, K. Wang, M. Choudhury, and P. J. G. Teunissen. 2018. "Multi-GNSS PPP-RTK: From Large- to Small-Scale Networks." *Sensors (Basel)* 18 (4): 1078. https://doi.org/10.3390/s18041078.

Psychas, D., A. Khodabandeh, and P. J. G. Teunissen. 2021. "Impact and Mitigation of Neglecting PPP-RTK Correctional Uncertainty." *GPS Solutions* 26 (1): 33. https://doi.org/10.1007/s10291-021-01214-y.

Psychas, D., S. Verhagen, X. Liu, Y. Memarzadeh, and H. Visser. 2019. "Assessment of Ionospheric Corrections for PPP-RTK Using Regional Ionosphere Modelling." *Measurement Science and Technology* 30 (1): 014001. https://doi.org/10.1088/1361-6501/aaefe5.

Rovira-Garcia, A., C. C. Timoté, J. M. Juan, J. Sanz, G. González-Casado, I. Fernández-Hernández, R. Orus-Perez, and D. Blonski. 2021. "Ionospheric Corrections Tailored to the Galileo High Accuracy Service." *Journal of Geodesy* 95 (12): 130. https://doi.org/10.1007/s00190-021-01581-x.

Saastamoinen, J. 1972. "Contributions to the Theory of Atmospheric Refraction." *Bulletin Géodésique* 105 (1): 279–298. https://doi.org/10.1007/BF02521844.

Tao, A.-L., and S.-S. Jan. 2015. "Wide-Area Ionospheric Delay Model for GNSS Users in Middle- and Low-Magnetic-Latitude Regions." *GPS Solutions* 20 (1): 9–21. https://doi.org/10.1007/s10291-014-0435-z.

Teunissen, P. J. G. 1995. "The Least-Squares Ambiguity Decorrelation Adjustment: A Method for Fast GPS Integer Ambiguity Estimation." *Journal of Geodesy* 70 (1–2): 65–82. https://doi.org/10.1007/Bf00863419.

Teunissen, P. J. G., and A. Khodabandeh. 2014. "Review and Principles of PPP-RTK Methods." *Journal of Geodesy* 89 (3): 217–240. https://doi.org/10.1007/s00190-014-0771-3.

Teunissen, P. J. G., D. Odijk, and B. Zhang. 2010. "PPP-RTK : Results of CORS Network-Based PPP with Integer Ambiguity Resolution." *Journal of Aeronautics, Astronautics and Aviation* 42 (4): 223–230.

Verhagen, S., and P. J. G. Teunissen. 2012. "The Ratio Test for Future GNSS Ambiguity Resolution." *GPS Solutions* 17 (4): 535–548. https://doi.org/10.1007/s10291-012-0299-z.

Wang, N., Z. Li, B. Duan, U. Hugentobler, and L. Wang. 2020. "GPS and GLONASS Observable-Specific Code Bias Estimation: Comparison of Solutions from the IGS and MGEX Networks." *Journal of Geodesy* 94 (8): 74. https://doi.org/10.1007/s00190-020-01404-5.

Wang, N., Y. Yuan, Z. Li, O. Montenbruck, and B. Tan. 2015. "Determination of Differential Code Biases with Multi-GNSS Observations." *Journal of Geodesy* 90 (3): 209–228. https://doi.org/10.1007/s00190-015-0867-4.

Wu, J., S. Wu, G. Hajj, W. Bertiguer, and S. Lichten. 1993. "Effects of Antenna Orientation on GPS Carrier Phase Measurements." *Manuscripta Geodaetica* 18 (2): 91–98. https://doi.org/10.1007/BF03655303.

Wübbena, G., M. Schmitz, and A. Bagge. 2005. "PPP-RTK: Precise Point Positioning Using State-Space Representation in RTK Networks." Paper presented at the 18th International Technical Meeting, ION GNSS, Long Beach, California, September 13–16.

Xu, C., Y. Jiang, Y. Gao, and Y. Yao. 2023. "Tropospheric Polynomial Coefficients for Real-Time Regional Correction by Kalman Filtering from Multisource Data." *Geo-Spatial Information Science*: 1–20. https://doi.org/10.1080/10095020.2023.2251530.

Yuan, Y., C. C. Tscherning, P. Knudsen, G. Xu, and J. Ou. 2008. "The Ionospheric Eclipse Factor Method (IEFM) and Its Application to Determining the Ionospheric Delay for GPS." *Journal of Geodesy* 82 (1): 1–8. https://doi.org/10.1007/s00190-007-0152-2.

Zha, J., B. Zhang, T. Liu, and P. Hou. 2021. "Ionosphere-Weighted Undifferenced and Uncombined PPP-RTK: Theoretical Models and Experimental Results." *GPS Solutions* 25 (4): 135. https://doi.org/10.1007/s10291-021-01169-0.

Zhang, B., Y. Chen, and Y. Yuan. 2018. "PPP-RTK Based on Undifferenced and Uncombined Observations: Theoretical and Practical Aspects." *Journal of Geodesy* 93 (7): 1011–1024. https://doi.org/10.1007/s00190-018-1220-5.

Zhang, B., P. J. G. Teunissen, and D. Odijk. 2011. "A Novel Un-Differenced PPP-RTK Concept." *The Journal of Navigation* 64 (S1): S180–S191. https://doi.org/10.1017/s0373463311000361.

Zhang, X., X. Ren, J. Chen, X. Zuo, D. Mei, and W. Liu. 2022. "Investigating GNSS PPP–RTK with External Ionospheric Constraints." *Satellite Navigation* 3 (1): 6. https://doi.org/10.1186/s43020-022-00067-1.

Zhu, H., J. Yu, Y. Dai, Y. Zhu, and Y. Huang. 2022. "Ionosphere Tomographic Model Based on Neural Network with Balance Cost and Dynamic Correction Using Multi-Constraints." *Atmosphere* 13 (3): 426. https://doi.org/10.3390/atmos13030426.